Diamond & Related Materials 92 (2019) 168–173

Contents lists available at ScienceDirect

Diamond & Related Materials

journal homepage: www.elsevier.com/locate/diamond

Cross-sectional transmission electron microscopy studies of boron ion implantation in hexagonal boron nitride

E. Aradi[a,*], S.R. Naidoo[b], F. Cummings[c], I. Motochi[d], T.E. Derry[b]

[a] School of Computing and Engineering, University of Huddersfield, Queensgate, Huddersfield HD1 3DH, United Kingdom
[b] DST/NRF Centre of Excellence in Strong Materials and the School of Physics, University of the Witwatersrand, Private Bag 3, Johannesburg, South Africa
[c] Electron Microscope Unit, University of the Western Cape, Private Bag X17, Bellville 7535, South Africa
[d] School of Science and Information Sciences, Maasai Mara University, P.O Box 861-20500, Narok, Kenya

ARTICLE INFO

Keywords:
Boron nitride
Transmission electron microscopy
Ion implantation

ABSTRACT

We have reported on the implantation of boron ion into hexagonal boron nitride (*h*-BN) material to aid the nucleation of cubic boron nitride nanocrystals (nc-BN).Single crystal *h*-BN was implanted with boron ion at 150 keV at fluences of the order of 10^{15} and 10^{17} ions/cm^2 at room temperature. High Angle Annular Dark-Field Scanning Transmission Electron Microscopy (HAADF-STEM) mapping showed a variation in image contrast in samples irradiated to a fluence of 1×10^{15} ions/cm^2. As predicted by Stopping Range and Ions in Materials (SRIM) calculations, the implanted region with the highest damage density appeared to have a bright contrast in HAADF-STEM which represented the high density *c*-BN symmetry. High Resolution Transmission Electron Microscopy (HRTEM) and electron diffraction measurements showed regions with nc-BN for samples implanted with low fluences and amorphous BN after implantation with high fluences indicating a fluence-related phase transition in BN. Raman spectroscopy showed the emergence of longitudinal optical frequency mode associated with *c*-BN after implantation.

1. Introduction

The search for materials with unique properties continues unabated due to increasing demand, especially in the modern high temperature-high frequency microelectronic device fabrication, coating materials for heavy duty applications, optical device fabrication, the abrasive sub-sector and the beauty and fashion industries. Diamond and its composites have been widely used over the years for most of the above mentioned applications. Unfortunately, these materials are not appropriate for some applications such as machining tools made of ferrous alloys, due to the high chemical reactivity of C to Fe at elevated temperature temperatures [1–5]. As such, the possibility of synthesizing materials with ultrahardness and properties similar or superior to diamond has become of great interest to the Material Science community. Over the years, this search has indicated that to synthesize stable materials which have hardness greater than or equal to diamond is a great challenge. Research is therefore being focused on the synthesis of materials with phases that are almost as hard as diamond, but with possibly other qualities that are superior to diamond in other respect.

Cubic BN is an important material because of its properties such as super hardness 75 GPa [6–8] high thermal stability for temperatures up to 2700 °C, thermal conductivities of about 13 W/m K and low dielectric constant [9–12]. It is a better semiconductor as compared to diamond and other commonly used semiconductors such as Si and GaN including, wide indirect band gap of 6.5 eV, can be doped as a shallow *p*-type semiconductor with Be and Mg and as an *n*-type with Si and Zn [13,14]. It is inert with regards to ferrous materials even at high temperatures while diamond forms iron carbide at about 600 °C [3,5].These properties have motivated the use of *c*-BN in numerous industrial, chemical and electrical applications [15–18].

Hexagonal boron nitride (*h*-BN), one of the allotropes of BN, has been used as a significant starting material for the nucleation of the cubic BN material [19,20]. Theory and experimental studies have shown that introducing defects into *h*-BN induces stress levels that may be responsible for the symmetry change into *c*-BN and other BN polymorphs. Mosuang et al. [21] in their study using a*b-initial* Local Density Approximations predicted that simple defects introduced into *h*-BN could facilitate a low activation energy for the formation of *c*-BN. Jimenez et al. [22] reported that 2 keV Ar ions at a fluence of 2×10^{17} ions/cm^2 led to a significant proportion of sp^3 characteristics found in *c*-BN. Hu et al. [23] obtained pure *c*-BN by implanting 30 keV N at a fluence of the order of 10^{18} ions/cm^2. Machakaet al. [24]

* Corresponding author.
E-mail address: e.aradi@hud.ac.uk (E. Aradi).

https://doi.org/10.1016/j.diamond.2018.12.020
Received 7 September 2018; Received in revised form 20 December 2018; Accepted 20 December 2018
Available online 21 December 2018
0925-9635/

in their study found that He ions implanted at 200 keV and fluences up to 10^{18} ions/cm^2 resulted in a *h*-BN to *c*-BN symmetry changes with traces of rhombohedral polymorph (*r*-BN) also detected after implantation. Lehtinen et al. [25] irradiated medium energy Ar into BN nanotubes and found that by varying the fluence, the material transformed into either *c*-BN nanocrystals or to amorphous (α-BN). Cataldo et al. [26] showed that neutron induced damage led to a hybridization change from sp^2 to sp^3 and also a certain degree of amorphization at high fluences. Ion induced phase transition have also been reported in phase transformation of other materials. Derry et al. [27] showed an increase in hardness values of *h*-BN after implantation with different ions. The transition of graphite to diamond by ion implantation has been reported in [28]. By ion implantation, lattice disordering and amorphization has been observed in TiN [29], ZrN [30], Cu_3N [31] and GaN (200 MeV Au ions) [32]. In this work we use moderate energy B ion implantation as a technique to promote *h*-BN to *c*-BN nucleation and characterize samples using TEM.

2. Experimental

Single crystal *h*-BN samples, supplied by HQ Graphene (http://www.hqgraphene.com/h-BN.php) were used as substrate/starting materials in this work. The samples were ~2 mm^2 flakes with thickness of approximately 500 μm.

Damage distribution was simulated using the *Stopping Range of Ions in Matter* (SRIM-2013) Monte Carlo computer code [33]. Damage density was calculated with the method used by [34] using the detailed damage calculation option of SRIM up to 2000 ions. The displacement energies were set at 15 eV for boron and 14 eV for nitrogen and with lattice and surface binding energies set to 0 eV and the sample thickness set to 700 nm.

Ion implantation was used as a method to introduce B ions into *h*-BN at 150 keV and to a maximum fluence of 1×10^{17} ions/cm^2 at a dose rate of $\approx 10^{13}$ ions/*s* at room temperature. A Varian 200-20A2F ion implanter [35] located at iThemba LABS (Gauteng), in Johannesburg, was used for the implantation experiments. Boron ions were obtained from boron trifluoride gas ionized in the ion source chamber of the ion implanter and selected by the implanter's mass analyser magnet.

To obtain electron transparent samples for cross-section TEM measurements, the samples were prepared by the focused ion beam sectioning (FIB) method, using a FEI Helos 650 Nanolab, fitted with a Ga ion beam source for milling and polishing. A gas injection system utilizing C gas precursor gas was used for attachment of lamellae to the grid. Special care was taken during thinning and polishing (10 pA final thinning current) to minimize any beam induced damage to the specimen.

Due to low doses used in this experiments, the sp^3 coordinated regions may be limited or sparingly distributed within the *h*-BN matrix making conventional TEM analysis challenging [36,37] except under very high magnification as used in HRTEM here. The High-Angle Annular Dark-field (HAADF) analyses that operate in the Scanning Transmission Electron Microscopy (STEM) mode was employed to characterize the microstructure of the sample since the contrast of the image correlates strongly with the sample's density [38]. This method is important in visualizing stress regions and identifying defects, ad-atoms and impurities with different weights from the surrounding pristine material. The materials/regions in the material with high density have a high contrast as compared to the low density regions. The HAADF STEM uses high incoherent, elastically scattered electrons to record images with different atoms giving different Z contrast/intensity.

The samples were analysed using high angle annular dark field scanning transmission electron microscopy (HAADF-STEM), high resolution TEM (HRTEM) and Raman spectroscopy. The FEI Quanta F20 TEM located at the University of the Western Cape, South Africa was used for all the TEM analyses. All experiments were conducted at 200 kV using a probe size of 0.19 nm. For HAADF analyses, a Fischione scintillator-photomultiplier HAADF detector, fitted into the wide-angle port located just below the final lens and above the projection chamber of the S-TWIN column of the microscope. The STEM imaging was done using a 60 μm C2 aperture, which yields a narrow convergence angle (α) of 10 mrad, and a camera length of 220 mm. Since no EELS experiments were conducted, the collection semi-angles (β) were not considered as only the high angular scattered electrons (both elastic and inelastic) are used for HAADF imaging. Hence it was not necessary to record the collection semi-angle.

Room temperature Raman spectroscopy measurements were carried out using the Horiba Jobin-Yvon Raman Spectrometer, located at the Microscopy Unit, University of the Witwatersrand. The 1800 groove/mm grating and a nitrogen cooled CCD detector were used, and the results analysed by interfaced PC software. The absorption coefficient (α) is used to determine the laser penetration depth (p), using the relationship $p = \alpha^{-1}$. Therefore, a 1 μm penetration depth p for the 514 nm (2.14 eV) photon with a 20 mW power was sampled with $\alpha_{h\text{-}BN}$ in the order of 10^4 cm^{-1} [36,39].

3. Results

3.1. HAADF-STEM and HRTEM

Fig. 1 represents HAADF STEM image for *h*-BN specimens (a) unimplanted and (b) implanted with B at 150 keV and a fluence of 1×10^{15} ions/cm^2, showing a cross-sectional length of about 700 nm from the sample's surface (region below platinum layer). Fig. 1(c) and (d) are the corresponding electron intensity profile (plotted using ImageJ (FIJI) software [40]) across the samples' surfaces indicated by the blue lines in a and b, while Fig. 1(e) represents the SRIM calculations for the damage density profile for B implanted *h*-BN at 150 keV with equivalent fluence, from the surface to the end of range of implantation.

The bright spots in the unimplanted image in Fig. 1(a) may be due to damage from Ga ions used in FIB sample preparation. Region 1 shown in Fig. 1(b), about 100 nm from the surface shows a low contrast region while region 2, which is about 400 nm below the surface shows a bright contrast. Region 1 corresponds to the region 1 in SRIM Fig. 1(e) which is a region of low damage density. Since low contrast represents regions with low density we suggest that region 1 is composed mostly of the low density sp^2 bonded *h*-BN. The high contrast in region 2 indicates a higher density in the material, which we attribute to be composed of some sp^3 bonded high density *c*-BN. The width of this region is approximately 100 nm which corresponds to the region with maximum implantation damage highlighted as the shaded region under the curve in SRIM in Fig. 1(e) about 400 nm below the samples surface. Therefore, we attribute the changes in *h*-BN resulting to *c*-BN symmetry change to be maximum within the implanted region. The corresponding electron intensity profiles are consistent with the differences in the contrast changes across the samples with the unimplanted profile showing a relatively constant electron intensity with depth while the implanted profile shows an increased intensity at about 400 nm corresponding to the implanted region.

Fig. 2 represents the HRTEM images for *h*-BN sample implanted to a fluence of 1×10^{15} ions/cm^2. Fig. 2(a) is the image taken 700 nm below the surface of the material. The image shows lattice fringes with lattice spacing of 0.255 ± 0.005 nm, which matches the lattice parameter of *h*-BN [41,42]. The inset represents the selected area diffraction pattern for *h*-BN in the {0002} plane. From SRIM, this area is beyond the implanted region therefore it is expected that the region is composed of mainly pristine *h*-BN agreeing well with the HRTEM images. Fig. 2(b) represents the HRTEM image taken 350 nm below the surface. This region corresponds to region 2 in both SRIM and HAADF images (Fig. 1), which are the regions with maximum damage and of low contrast respectively. The lattice parameter for the region (indicated by the arrow) is about 0.310 ± 0.005 nm which corresponds to the lattice parameter for *c*-BN [13], suggesting that this region contains nc-BN.

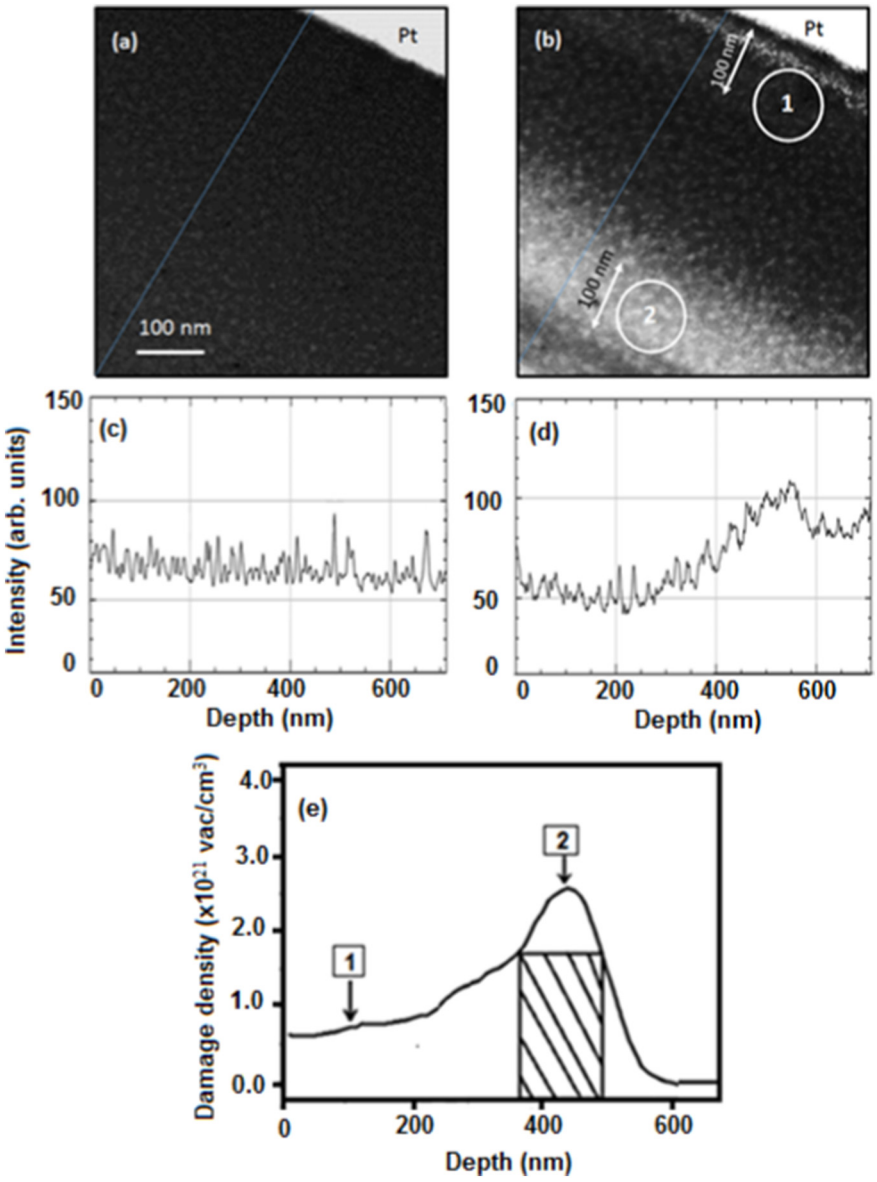

Fig. 1. HAADF STEM micrograph for single crystal *h*-BN (a) unimplanted and (b) implanted with B at 1.5×10^{15} ions/cm^2 and 150 keV (c and d) corresponding surface plot for unimplanted and irradiated samples respectively and (e) SRIM simulation showing the damage profile for *h*-BN sample implanted with 150 keV B ions to a fluence of 1×10^{15} ions/cm^2. The highlighted region represents the region with the maximum damage. (Scale bar in (a) applies for both micrographs).

The big lattice fringes in Fig. 2(b) are Moiré fringe due to crystal overlap. The selected area diffraction pattern (SADP) of this region could not reveal any difference in the diffraction pattern (DP) compared to *h*-BN, probably due to minute size of the region, therefore, the nano-beam diffraction (NBD) mode was used to acquire DP from specific areas in the implanted region and the inset in Fig. 2(b) shows a cubic NBDP in the {111} plane for *c*-BN taken within the highlighted region.

3.2. Raman measurements

Fig. 3(a) represents the Raman measurements of unimplanted single crystal *h*-BN sample. The spectrum illustrates a Raman phonon mode signal centred at 1367 cm^{-1}. This feature represents the high-energy E_{2g} symmetry Raman-active phonon mode which arises from the in-plane B—N bond stretching within the basal plane [36,43]. Fig. 3(b) represents the Raman spectrum for the sample implanted with 150 keV B to a fluence of 1.5×10^{15} ions/cm^2. Together with the phonon peak at 1367 cm^{-1}, there occurs a new feature centred at 1298 cm^{-1}.This features has a distinctively lower intensity and a more asymmetric line broadening than the principal *h*-BN line.

Raman measurements under similar conditions of temperature and energy for different fluences have been reported in [37,44]. The Raman lineshape and position for *c*-BN will vary depending of the size of the crystals being analysed. Cubic BN with size > 500 nm shows two phonon modes: the Transverse Optical (TO) line which occurs at ~1057 cm^{-1} and the Longitudinal Optical (LO) line which occurs at ~1305 cm^{-1} [45]. If the *c*-BN contains micron and nano-size crystals, the Raman spectrum will display a TO mode at 1057 cm^{-1} and LO modes at 1305 cm^{-1} with an unstructured broad feature located near the LO phonon mode centred around 1290 cm^{-1}. When the specimen is made of nanocrystals (< 100 nm) the TO mode for *c*-BN disappears, while the LO mode peak broadens and shifts to a frequency of about 1290 cm^{-1}.The experimental measurements and analyses for the changes in c-BN Raman lineshape for c-BN with various particle sizes have been carried out and discussed in previous work [36]. Parayanthal et al. [46] using the Spatial Correlation Model (SCM) explained the effect of particle size on the changes in the Raman lineshape broadening and symmetry. Similar changes in the Raman lineshape have been

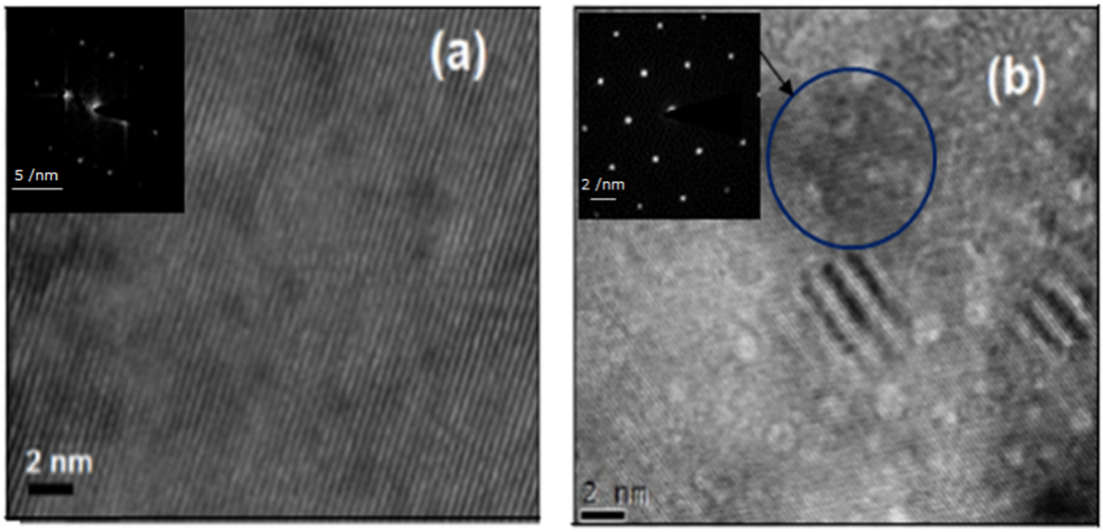

Fig. 2. HRTEM images taken for h-BN sample implanted to a fluence of a 1×10^{15} ions/cm^2. (a) 700 nm below the surface and (b) 350 nm below the surface of the sample. The insets are the SADP and the NBDP for the respective regions. (The insets in (a) shows the DP in the {0002} plane while that of (b) shows some the {111} c-BN plane within the highlighted region of the specimen). This imply that damage was up to and beyond the 350 nm level but not reaching 700 nm.

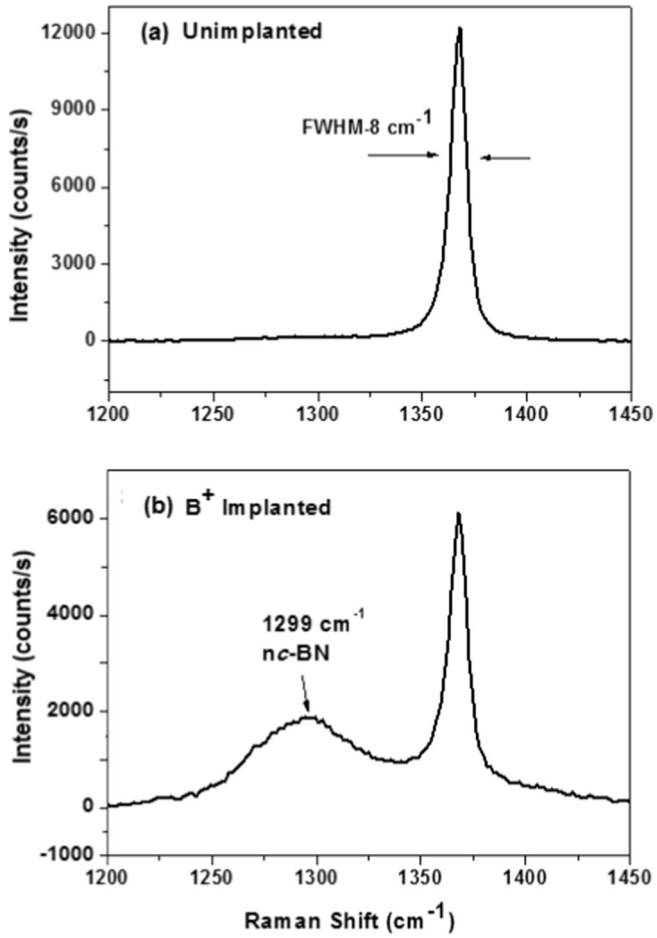

Fig. 3. Raman spectra for *h*-BN samples (a) unimplanted and (b) implanted with B at 1.5×10^{15} ions/cm^2 and the energy of 150 keV at room temperature. (There is broadening of the peak at approx. 1360 cm^{-1} implying disorder and another broad peak centred at 1298 cm^{-1} implying formation of sp^3 hybridization).

reported for GaN [47] and diamond with varying crystal sizes [48]. We therefore attribute the new Raman feature to nc-BN.

High fluence implantation.

Fig. 4(a) represents the Raman spectroscopy and SADP taken for samples implanted with 150 keV B to a fluence of 1×10^{17} ions/cm^2. The Raman spectra shows the high frequency *h*-BN peak at 1364 cm^{-1}, having shifted by 2 cm^{-1}from the pristine sample. The shift to lower wavenumber has been associated with introduction of compressive stress in the material [49]. A new peak located at 1294 cm^{-1} is also present with a broader linewidth and a lower intensity as compared to the samples implanted to a fluence of 1×10^{15} ions/cm^{2}in Fig. 3(b).

Fig. 4(b) is the HRTEM image for the same sample taken within the implanted region, indicated by the continuous red arrow and within the region beyond the implanted range indicated by the green broken arrow. The image show a loss of the ordered lattice fringes in the region with the maximum implantation while the region beyond the implanted range exhibits the lattice fringes with lattice parameter of 0.255 ± 0.005 nm corresponding to *h*-BN. The insets in Fig. 4(b) are the SADP taken at the respective areas. The SADP taken at the implanted region shows amorphous rings synonymous to amorphous (α)-BN. The SADP beyond the implanted region shows the {0002} reflection for *h*-BN. This implies that at this fluence the effect of irradiation is to induce amorphization due to increased stress in the sample. The fluence dependence of the formation of nc-BN has been observed in previous work for B and other ions with the threshold fluence for nucleation for B implantation being in the order of 10^{15} ions/cm^2 [44,50].Other studies have also shown that *c*-BN was not detected at fluences of the order if 10^{18} ions/cm^2 with *h*-BN as a starting material [24,51].

4. Discussions

The modifications that occur in *h*-BN resulting in the formation of *c*-BN nanocrystals reported here are suggested to occur due to the accumulation of point defects as created by B implantation. When energetic ions are implanted into the *h*-BN lattice they collide with the primary atoms displacing them from their equilibrium lattice position creating either a vacancy or by temporarily settling in the interstitial site within the interplanar space of the material [52]. This leads to a large concentration defect within the matrix. The accumulation of defects and the alteration of the lattice create high stress/strain level in *h*-BN. The midplane defects and the subsequent stress they cause induces

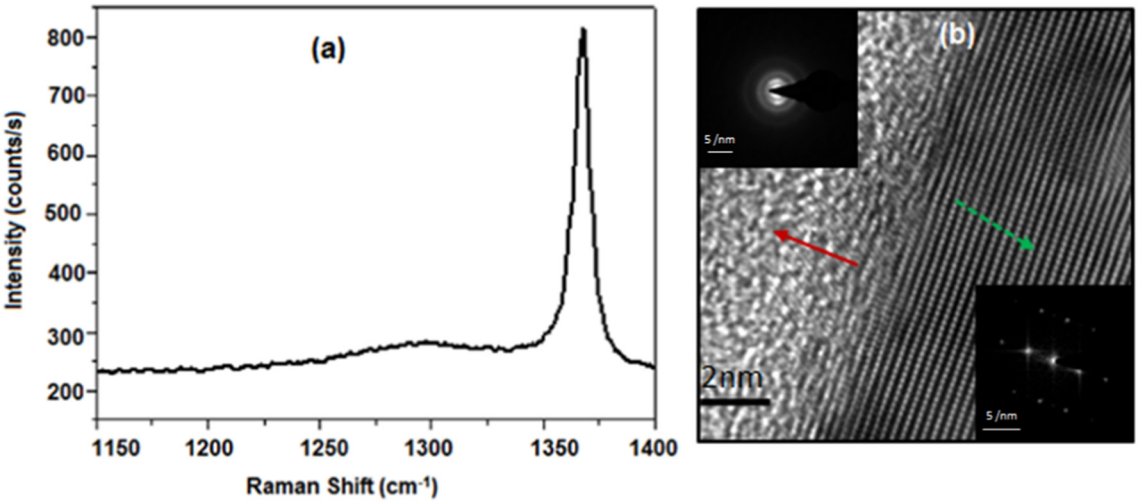

Fig. 4. (a) Raman spectra for 150 keV B implanted sample at a fluence of 1×10^{17} ions/cm^2 (b) HRTEM micrograph of the same sample. The red arrow shows the implanted region and the green broken arrow show the region beyond the implanted range. The insets in (b) represent the SADP for the respective regions. (For interpretation of the references to colour in this figure legend, the reader is referred to the web version of this article.)

significant amount of breaking and buckling of the weak van der Waal bonds within the *h*-BN *c*-planes. The continuous breaking and buckling of the weak *Van der Waal* bonds and the basal B_3N_3 honeycomb hexagon bond-stretching increases the bond length resulting in an increase in the local density of the material.

The breaking of interplanar bonds leads to a change in the electron density in the interatomic and interlayer spaces. The electron density between the B and N atom in adjacent planes increase, leading to a decrease in the interlayer spacing and lowering of the formation energy for *c*-BN. The B_3N_3 honeycombs buckle into a cubic-chair structure which favour a nonplanar steric covalent bond reconstruction of the atoms in the adjacent planes. The bonding network now changes to a 3-dimensional tetrahedral structure with sp^3 hybridization synonymous to the high density *c*-BN which is detected by Raman as a new *c*-BN phonon mode and in HRTEM within the implanted region.

The changes in observed *h*-BN as a function of fluence indicate that there is a critical fluence for *c*-BN nucleation. Beyond this fluence the effect of the increased defect concentration is to induce a complete loss in the long range order leading to amorphization of the material.

5. Conclusion

In summary, 150 keV B ion implantation with fluences of the order of 1×10^{15} ions/cm^2 induced a phase change of *h*-BN to nano-regions with *c*-BN. These originated from the existence of defects-induced stress introduced by interplane interstitial in *h*-BN. High Angle Annular Dark-Field STEM established regions with bright contrast which represented the high density nc-BN which were localized within the implanted region. High resolution TEM showed regions with lattice parameter corresponding to *c*-BN for implantation carried out with a fluence of 1×10^{15} ions/cm^2 and amorphous regions for implantation carried out with 1×10^{17} ions/cm^2. Raman Spectroscopy showed evolution of broad peaks located at the LO-*c*-BN wavenumbers after implantation representative of *c*-BN with nano-size crystals, with this peak degrading with increasing fluence.

Acknowledgement

The financial support from DST-NRF Centre of Excellence in Strong Materials and the University of the Witwatersrand is highly appreciated. Many thanks to the iThemba LABS Gauteng for the implanter facility.

References

[1] A.K. Wolfrum, B. Matthey, A. Michaelis, M. Herrmann, On the stability of c-BN-reinforcing particles in ceramic matrix materials, Materials (Basel) 11 (2018) 1–17.
[2] F.P. Bundy, Superhard Mater. (1974) 1.
[3] Z.J. Li, F.Z. Fang, H. Gong, X.D. Zhang, Review of diamond-cutting ferrous metals, Int. J. Adv. Manuf. Technol. 68 (5–8) (2013) 1717–1731.
[4] V.K. Starkov, S.A. Rybtsev, E.G. Polkanov, O.S. Kiskin, Comparative analysis of performance of cubic boron nitride and microcrystallite alumina tools in profile grinding of form cutting, J. Superhard Mater. 36 (1) (2014) 43–45.
[5] J. Angseryd, M. Elfwing, E. Olsson, H.O. Andrén, Detailed microstructure of a cBN based cutting tool material, Int. J. Refract. Met. Hard Mater. 27 (2) (2009) 249–255.
[6] Z. Zhao, B. Xu, Y. Tian, Recent advances in superhard materials, Annu. Rev. Mater. Res. 46 (1) (2016) 383–406.
[7] C. Chen, Z. Wang, T. Kato, N. Shibata, T. Taniguchi, Y. Ikuhara, Misfit accommodation mechanism at the heterointerface between diamond and cubic boron nitride, Nat. Commun. 6 (2015) 1–6.
[8] A. Mansouri Tehrani, L. Ghadbeigi, J. Brgoch, T.D. Sparks, Balancing mechanical properties and sustainability in the search for superhard materials, Integr. Mater. Manuf. Innov. 6 (1) (2017) 1–8.
[9] X. Liu, X. Chen, H. Ma, X. Jia, J. Wu, T. Yu, Y. Wang, J. Gao, S. Petitgirard, C.R. Bina, S.D. Jacobsen, Ultrahard stitching of nanotwinned diamond and cubic boron nitride in C 2-BN composite, Sci. Rep. 6 (2016) 1–9.
[10] Y. Liu, P. Jin, A. Chen, H. Yang, Y. Xu, Residual compressive stress induced infrared-absorption frequency shift of hexagonal boron nitride in cubic boron nitride films prepared by plasma-enhanced chemical vapor deposition, J. Appl. Phys. 112 (5) (2012) 0–5.
[11] W.J. Zhang, I. Bello, Y. Lifshitz, S.T. Lee, Recent advances in cubic boron nitride deposition, Small 4 (2003) 184–188.
[12] C.B. Samantaray, R.N. Singh, Review of Synthesis and Properties of Cubic Boron Nitride (c-BN) Thin Films, 50 (2005) (no. 6).
[13] N. Izyumskaya, D.O. Demchenko, S. Das, Ü. Özgür, V. Avrutin, H. Morkoç, Recent development of boron nitride towards electronic applications, Adv. Electron. Mater. 3 (5) (2017) 1–22.
[14] H. Park, T.K. Kim, S.W. Cho, H.S. Jang, S.I. Lee, S.Y. Choi, Large-scale synthesis of uniform hexagonal boron nitride films by plasma-enhanced atomic layer deposition, Sci. Rep. 7 (2017) 1–8.
[15] A. Khanaki, et al., Self-assembled cubic boron nitride nanodots, Sci. Rep. 7 (1) (2017) 1–10.
[16] W.J. Zhang, Y.M. Chong, B. He, I. Bello, S.T. Lee, Cubic Boron Nitride Films: Properties and Applications, 3 Elsevier Ltd, 2014.
[17] A. Rabinkin, A.E. Shapiro, M. Boretius, Brazing of Diamonds and Cubic Boron Nitride, Woodhead Publishing Limited, 2013.
[18] X.W. Zhang, Doping and electrical properties of cubic boron nitride thin films: a critical review, Thin Solid Films 544 (2013) 2–12.
[19] F.P. Bundy, R.H. Wentorf, Direct transformation of hexagonal boron nitride to denser forms, J. Chem. Phys. 38 (5) (1963) 1144–1149.
[20] H. Hofsäss, H. Feldermann, M. Sebastian, C. Ronning, Thresholds for the phase formation of cubic boron nitride thin films, Phys. Rev. B 55 (19) (1997) 13230–13233.
[21] T.E. Mosuang, J.E. Lowther, Influence of defects on the h-BN to c-BN transformation, Phys. Rev. B: Condens. Matter Mater. Phys. 66 (1) (2002) 141121–141125.
[22] I. Jiménez, A. Jankowski, L. Terminello, D. Sutherland, J. Carlisle, G. Doll, Core-level photoabsorption study of defects and metastable bonding configurations in boron nitride, Phys. Rev. B: Condens. Matter Mater. Phys. 55 (18) (1997) 12025–12037.

[23] C. Hu, Q.M.J. Wu, J. Shen, S. Kotake, Y. Suzuki, Cubic BN formation by ion implantation, Thin Solid Films 402 (1–2) (2002) 117–120.
[24] R. Machaka, R.M. Erasmus, T.E. Derry, Formation of cBN nanocrystals by He+ implantation into hBN, Diam. Relat. Mater. 19 (10) (2010) 1131–1134.
[25] O. Lehtinen, E. Dumur, J. Kotakoski, A.V. Krasheninnikov, K. Nordlund, J. Keinonen, Production of defects in hexagonal boron nitride monolayer under ion irradiation, Nucl. Instrum. Methods Phys. Res., Sect. B 269 (11) (2011) 1327–1331.
[26] F. Cataldo, S. Iglesias-Groth, Neutron damage of hexagonal boron nitride: h-BN, J. Radioanal. Nucl. Chem. 313 (1) (2017) 261–271.
[27] T.E. Derry, L.I. Lisema, A.T. Magabe, E. Aradi, R. Machaka, M. Madhuku, Allotrope conversion and surface hardness increase in ion implanted boron nitride, Surf. Coat. Technol. 355 (2018) 61–64.
[28] F. Banhart, The transformation of graphitic onions to diamond under electron irradiation, J. Appl. Phys. 81 (8) (1997) 3440–3445.
[29] M. Popović, M. Novaković, M. Mitrić, K. Zhang, N. Bibić, Structural, optical and electrical properties of argon implanted TiN thin films, Int. J. Refract. Met. Hard Mater. 48 (2015) 318–323.
[30] S. Khan, I. Ahmed, N. Khalid, M. Mehmood, A. Waheed, M. Malik, Carbon ions irradiation induced modifications in structural and electrical resistivity characteristics of ZrN thin films, Mater. Sci. Semicond. Process. 39 (2015) 530–535.
[31] N. Matsunami, H. Kakiuchida, M. Tazawa, M. Sataka, H. Sugai, S. Okayasu, Electronic and atomic structure modifications of copper nitride films by ion impact and phase separation, Nucl. Instrum. Methods Phys. Res., Sect. B 267 (16) (2009) 2653–2656.
[32] N. Matsunami, T. Teramoto, S. Okayasu, M. Sataka, B. Tsuchiya, Modifications of WN x O y films by ion impact, Surf. Coat. Technol. (June 2018) 2–7 (Available online).
[33] J.F. Ziegler, M.D. Ziegler, J.P. Biersack, SRIM – the stopping and range of ions in matter (2010), Nucl. Instrum. Methods Phys. Res., Sect. B 268 (11–12) (2010) 1818–1823.
[34] R.E. Stoller, M.B. Toloczko, G.S. Was, A.G. Certain, S. Dwaraknath, F.A. Garner, On the use of SRIM for computing radiation damage exposure, Nucl. Instrum. Methods Phys. Res., Sect. B 310 (2013) 75–80.
[35] G.J. Phelps, Dopant ion implantation simulations in 4H-silicon carbide, Model. Simul. Mater. Sci. Eng. 12 (6) (2004) 1139–1146.
[36] E. Aradi, S.R. Naidoo, R.M. Erasmus, B. Julies, T.E. Derry, Raman studies on the effect of multiple-energy ion implantation on single-crystal hexagonal boron nitride, Radiat. Eff. Defects Solids 170 (3) (2015) 1.
[37] E. Aradi, S.R. Naidoo, R.M. Erasmus, B. Julies, T.E. Derry, Investigations on the characterization of ion implanted hexagonal boron nitride, Nucl. Instrum. Methods Phys. Res., Sect. B 307 (2013).
[38] S. Utsunomiya, R.C. Ewing, Application of high-angle annular dark field scanning transmission electron microscopy, scanning transmission electron microscopy-energy dispersive x-ray spectrometry, and energy-filtered transmission electron microscopy to the characterization of nanopar, Environ. Sci. Technol. 37 (4) (2003) (786–79).
[39] S. Reich, A.C. Ferrari, R. Arenal, A. Loiseau, I. Bello, J. Robertson, Resonant Raman scattering in cubic and hexagonal boron nitride, Phys. Rev. B 71 (20) (2005) 205201.
[40] J. Schindelin, et al., Fiji: an open-source platform for biological-image analysis, Nat. Methods 9 (7) (2012) 676–682.
[41] N. Ooi, A. Rairkar, L. Lindsley, J.B. Adams, Electronic structure and bonding in hexagonal boron nitride, J. Phys. Condens. Matter 18 (1) (2006) 97–115.
[42] P.C. Mende, et al., Characterization of Hexagonal Boron Nitride Layers on Nickel Surfaces by Low-energy Electron Microscopy, 6 (2016).
[43] R. Geick, C. Perry, G. Rupprecht, Normal modes in hexagonal boron nitride, Phys. Rev. 146 (2) (1966) 543–547.
[44] E. Aradi, S.R. Naidoo, D.G. Billing, D. Wamwangi, I. Motochi, T.E. Derry, Ion beam modification of the structure and properties of hexagonal boron nitride: an infrared and X-ray diffraction study, Nucl. Instrum. Methods Phys. Res., Sect. B 331 (2014) 140–143.
[45] W.J. Zhang, Y.M. Chong, I. Bello, S.T. Lee, Nucleation, growth and characterization of cubic boron nitride (cBN) films, J. Phys. D. Appl. Phys. 40 (20) (2007) 6159–6174.
[46] P. Parayanthal, F.H. Pollak, Raman scattering in alloy semiconductors: 'spatial correlation' model, Phys. Rev. Lett. 52 (20) (1984) 1822–1825.
[47] Z. Feng, W. Wang, S. Chua, P. Zhang, K. Williams, G. Pitt, Raman scattering properties of GaN thin films grown on sapphire under visible and ultraviolet excitation, J. Raman Spectrosc. 32 (2001) 840–846.
[48] M. Chaigneau, G. Picardi, H.A. Girard, J.C. Arnault, R. Ossikovski, Laser heating versus phonon confinement effect in the Raman spectra of diamond nanoparticles, J. Nanopart. Res. 14 (6) (2012).
[49] R.M. Erasmus, J.D. Comins, T. Kubeka, Optical Spectroscopy Techniques for the NDT of Hard Materials, (2012), pp. 16–20.
[50] E. Aradi, R.M. Erasmus, T.E. Derry, Formation of c-BN nanoparticles by helium, lithium and boron ion implantation, Nucl. Instrum. Methods Phys. Res., Sect. B 272 (2012) 57–60.
[51] O. Lehtinen, et al., Ion irradiation of multi-walled boron nitride nanotubes, Phys. Status Solidi C 1259 (3) (2010) 1–4.
[52] I.J. Beyerlein, M.J. Demkowicz, A. Misra, B.P. Uberuaga, Defect-interface interactions, Prog. Mater. Sci. 74 (2015) 125–210.